



Article

Geostationary Full-Spectrum Wide-Swath High-Fidelity Imaging Spectrometer: Optical Design and Prototype Development

Jiacheng Zhu ^{1,2} , Zhicheng Zhao ^{1,2}, Quan Liu ^{1,2,*} , Xinhua Chen ^{1,2}, Huan Li ³, Shaofan Tang ³ and Weimin Shen ^{1,2}

¹ College of Optoelectronic Science and Engineering, Soochow University, Suzhou 215006, China

² Key Lab of Advanced Optical Manufacturing Technologies of Jiangsu Province & Key Lab of Modern Optical Technologies of Education Ministry of China, Suzhou 215006, China

³ Beijing Institute of Space Mechanics and Electricity, Beijing 100094, China

* Correspondence: liuquan@suda.edu.cn

Abstract: The optical system of an imaging spectrometer working on a geostationary earth orbit (GEO) covering a full optical spectrum of 0.3–12.5 μm is analyzed and designed. It enables a ground coverage of 400 \times 400 km by internal scanning and achieves a high spatial resolution of 25 m. The full spectrum is divided into five sub-bands, and each band adopts four spectrometers to splice in the field of view to achieve the ultra-long slit required by the wide swath. The total length of the slit is up to 241.3 mm. This paper focuses on compact spectrometers with long slits that can meet the splicing requirements and points out that low spectral distortions, low stray light, high signal-to-noise ratio, and uniform spectral response are necessary for high-fidelity performance. The Offner and Wynne–Offner high-fidelity spectrometers based on convex blazed gratings are designed, and prototypes of each band are developed as well. The properties of long slits and convex blazed gratings are presented. The maximum length of a single slit is 61.44 mm. The groove density of gratings for five bands ranges from 8.8 lp/mm to 312.1 lp/mm, and the peak efficiency is up to 86.4%. The alignment and test of the spectrometers are introduced. Results show that the developed spectrometers have high fidelity and fulfill all requirements.

Keywords: hyperspectral imaging; optical design; geostationary orbit; spectrometer; remote sensing



Citation: Zhu, J.; Zhao, Z.; Liu, Q.; Chen, X.; Li, H.; Tang, S.; Shen, W. Geostationary Full-Spectrum Wide-Swath High-Fidelity Imaging Spectrometer: Optical Design and Prototype Development. *Remote Sens.* **2023**, *15*, 396. <https://doi.org/10.3390/rs15020396>

Academic Editors: Siting Xiong, Yu Tao and Rui Song

Received: 28 November 2022

Revised: 4 January 2023

Accepted: 6 January 2023

Published: 9 January 2023



Copyright: © 2023 by the authors. Licensee MDPI, Basel, Switzerland. This article is an open access article distributed under the terms and conditions of the Creative Commons Attribution (CC BY) license (<https://creativecommons.org/licenses/by/4.0/>).

1. Introduction

Imaging spectrometers are widely used in the field of remote sensing because of their ability to obtain spatial and spectral information simultaneously. After the development in the 1980s and 1990s, a series of imaging spectrometers were applied on airborne platforms [1–6]. In the 21st century, this technology developed rapidly in the field of spaceborne hyperspectral remote sensing. Since the Earth observation satellite EO-1 carried the first spaceborne hyperspectral imager Hyperion [7,8] in 2000, many satellites have carried or planned to carry imaging spectrometers to execute Earth observation missions. Hyperspectral remote sensing plays a role in ocean and coast monitoring [9–12], environment monitoring [13], earth surface detection [14,15], mineral exploration [16], and military activities [17]. Hyperspectral imaging methods [18–21] and systems [22–25] have also developed rapidly. With the increasing demand for acquiring spatial and spectral information more efficiently and accurately, imaging spectrometers are driven towards faster response, larger width, higher resolution, and higher signal-to-noise ratio. Since the satellite on geostationary orbit has the unique advantage of keeping relatively stationary with the ground, it has high timeliness and continuous observation capability, thus it can obtain information from ground scenes quickly and widely. However, most of the spectral-type remote sensing payloads serving in geostationary orbit are multispectral payloads [26–28].

They have only a dozen spectral channels in full spectrum, which is not enough to obtain fingerprint information of ground scenes. Their ability to identify substances and components is far inferior to hyperspectral payloads. The research on hyperspectral payloads on geostationary orbit is also limited to some special spectral bands, focusing mainly on atmospheric monitoring [29–35].

The collection of full-spectrum hyperspectral data can significantly improve recognition accuracy and provide more target descriptions. The development of full-spectrum wide-swath imaging spectrometers is a current trend in hyperspectral remote sensing from geostationary orbit. However, due to the great difficulty and high cost of this method, there is little related research at present. In this paper, we present an optical system of the Geostationary Full-spectrum Wide-swath High-fidelity Imaging Spectrometer (GeoFWHIS). The principle of GeoFWHIS is described, and the optical design is explained. We focus on the study of the spectrometers from each sub-band and analyze their difficulties and requirements in order to realize high-fidelity spectral imaging. Finally, prototypes of spectrometers are developed and some test results are presented.

2. Principle and Method

Specifications of GeoFWHIS are shown in Table 1. Its wavelength range covers from near ultraviolet to long wavelength infrared (0.3–12.5 μm). The full spectrum is divided into five sub-bands, including the near-ultraviolet and visible band (B1-UVIS), the visible and near-infrared band (B2-VNIR), the short-wave infrared band (B3-SWIR), the medium wave infrared band (B4-MWIR), and the long wave infrared band (B5-LWIR). They have different specifications for spatial resolution, spectral resolution, modulation transfer function (MTF), and signal-to-noise ratio (SNR). To meet the different requirements of each band, a reasonable layout of the optical system is particularly important. The layout block diagram of GeoFWHIS is shown in Figure 1. It is composed of an afocal telescope, three imaging objectives, and spectrometers for five bands. The GeoFWHIS keeps relatively stationary with the ground, so its integral time will not be limited by the movement of the platform. Sufficient SNR can be achieved by actively increasing the integral time, to reduce the requirement of a large relative aperture. Meanwhile, GeoFWHIS cannot work in a push-broom manner such as LEO (Low Earth Orbit) imaging spectrometers because of the relatively stationary state. Imaging of a single scene covering 400×400 km is completed through internal scanning. The afocal telescopic compresses the incident light into a small aperture. At the telescope's exit pupil, the scanning mirror scans the compressed beam into the imaging objectives, and the full spectrum is divided into five sub-bands by dichroic mirrors. It can be seen from Table 1 that the GeoFWHIS has a wide swath and high spatial resolution. There are 16,000 spatial sampling points in B1 and B2 bands within 400 km, and the instantaneous field of view is up to $0.7 \mu\text{rad}$. Wide swath and high spatial resolution determine that the system has long slits; the longest is 241.3 mm. Such a long slit will result in a very large spectrometer, which poses great challenges to the manufacture of both the spectrometer and detector. Therefore, we use multiple spectrometers for each band to cover the super-long slit. According to the specifications of the selected detector, four spectrometers are spliced, and there is an overlap between every two adjacent spectrometers.

We compare the specifications between GeoFWHIS and some current satellite sensors in orbit in Table 2. The GEO meteorological satellite sensor GOES-R ABI (Advanced Baseline Imager), FY-4 AGRI (Advanced Geostationary Radiation Imager) and the LEO hyperspectral satellite sensor EO-1 Hyperion, GF-5 AHSI (Advanced Hyperspectral Imager), and EnMAP HSI (Hyperspectral Imager) are compared. Compared with the GEO meteorological satellite sensors, GeoFWHIS has significantly higher spatial and spectral resolution in the full spectrum. Its spatial and spectral resolution is more than one order of magnitude higher than ABI and AGRI. Compared with the LEO hyperspectral satellite sensors, GeoFWHIS has a wider swath width, a wider spectral range, and the same order of spatial and spectral resolution. Therefore, GeoFWHIS not only has the advantage of

wide coverage of GEO satellite sensors, but also the advantage of high resolution of LEO satellite sensors.

Table 1. Specifications and system parameters of GeoFWHIS.

Specifications and Parameters	Values				
Orbital altitude	geostationary orbit (~36,000 km)				
Swath width/km	400 × 400				
FOV	0.64° × 0.64°				
Entrance pupil diameter/m	3.2				
Band	B1 (UVIS)	B2 (VNIR)	B3 (SWIR)	B4 (MWIR)	B5 (LWIR)
Wavelength range/μm	0.3–0.56	0.55–1.01	1–2.5	3–5	8–12.5
Spatial resolution/m	25	25	50	50	100
Spectral resolution (FWHM)/nm	4	5	12	50	200
Spectral sampling distance/nm	4	5	12	50	200
MTF	0.17	0.17	0.17	0.12	0.12
Focal length/m	21.6	21.6	17.28	17.28	8.64
F number	6.75	6.75	5.4	5.4	2.7
Detector resolution	4096 × 2048	4096 × 2048	2048 × 256	2048 × 256	1024 × 256
Pixel size/μm	15 × 15	15 × 15	24 × 32	24 × 32	24 × 32
Pixels per spectral channel	6	6	2	3	3
Total length of slit/mm	241.3	241.3	193	193	96.5
Number of splicing spectrometers	4	4	4	4	4
Single slit length/mm	61.44	61.44	49.152	49.152	24.576
Slit width/μm	15	15	24	24	24

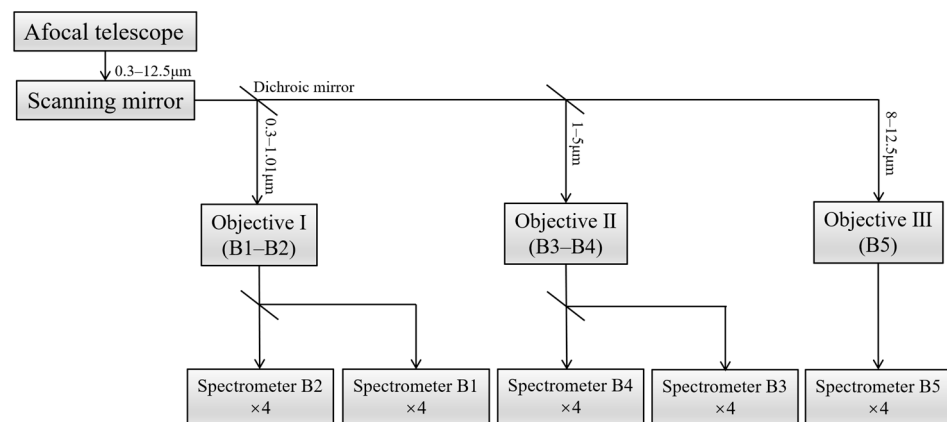


Figure 1. Layout block diagram of GeoFWHIS.

Table 2. Comparison of specifications between GeoFWHIS and some current satellite sensors in orbit.

Specifications	GEO			LEO		
	GeoFWHIS	GOES-R ABI [26]	FY-4 AGRI [36]	EO-1 Hyperion [8]	GF-5 AHSI [37]	EnMAP HIS [13]
Orbital altitude/km	36,000	36,000	36,000	705	705	650
Swath width/km	400	1000	1000	7.5	60	30
Wavelength range/μm	0.3–12.5	0.45–13.6	0.45–13.8	0.4–2.5	0.4–2.5	0.42–2.45
Spatial resolution/m	25–100	500–2000	500–4000	30	30	30
Spectral resolution/nm	4–200	15–1000	30–1000	10	5–10	5.5–11.5
Spectral channels	350	16	14	220	330	228

3. Optical Design and Analysis

There are two difficulties in the optical design of GeoFWHIS, one is to realize the full-spectrum imaging through integrated design. Since GeoFWHIS contains many optical

modules, and the specifications are different between each optical module. In the design process, all optical modules should meet the requirements of pupil matching and field matching. Therefore, in addition to ensuring the imaging quality, it is also necessary to ensure the pupil quality of the optical system, so as to facilitate the splicing and integration of each module. Another difficulty is designing long-slit compact spectrometers suitable for splicing. Generally, the spectrometer will become larger with the increase in its slit length, which makes it hard to splice. How to realize a long slit while keeping a compact structure is the primary problem to be solved in the spectrometer of GeoFWHIS. This section gives the design results and performance of each part of the system.

3.1. Fore-Optics

The afocal telescope and imaging objectives constitute the fore-optics of GeoFWHIS. Optical path diagram of the designed fore-optics is shown in Figure 2. Three objectives are arranged at the back of the telescope's primary mirror, and they share an entrance pupil which is also the telescope's exit pupil. The scanning mirror is located on this pupil and reflects the light into the objectives. Dichroic mirrors in the image space of objectives I and II subdivide spectral bands, and a total of five image planes for five bands are formed.

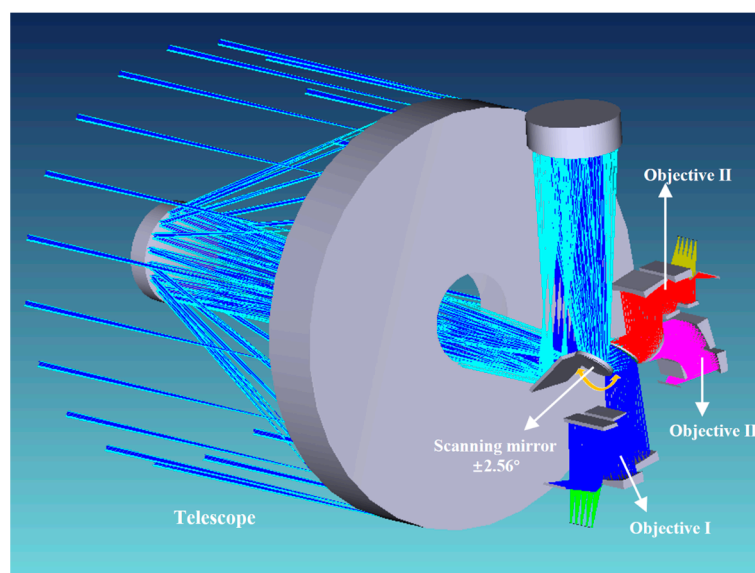


Figure 2. Optical path diagram of fore-optics.

The telescope's entrance pupil diameter is 3.2 m, and its field of view (FOV) is $0.64^\circ \times 0.64^\circ$. Compression ratio, i.e., the ratio of the entrance pupil diameter to the exit pupil diameter, is a crucial parameter of the telescope. The larger the compression ratio is, the smaller the obtainable exit pupil. However, the FOV in image space will increase, which will also increase the difficulty of designing imaging objectives. The compression ratio of the telescope is 16, the exit pupil diameter is 200 mm, and the FOV in image space is $10.24^\circ \times 10.24^\circ$. Considering the requirements of a large aperture and high compression ratio, we designed an afocal three-mirror anastigmatic telescope with zigzag axis [38]. Based on a coaxial three-mirror system, the three mirrors are slightly decentered and tilted to avoid secondary obscuration, and thus the exit pupil is led out. The optical path of the telescope is shown in Figure 3a. Its primary mirror is a paraboloid, and its second and third mirrors are hyperboloids. The line obscuration coefficient of the telescope is 0.22. A folding plane mirror is added in front of the middle image to fold the optical path. Wavefront quality of the telescope is close to the diffraction limit, and its RMS wavefront error is 0.024λ ($\lambda = 632.8 \text{ nm}$) at the center of the FOV, shown in Figure 3b. Three imaging objectives are mounted behind the telescope, each with an entrance pupil diameter of 200 mm, a linear FOV of 10.24° , and a focal length 16 times smaller than that of the GeoFWHIS, referring

to the focal lengths contained in Table 1. The off-axis three-mirror system is suitable for medium FOV and long focal length objectives. In this paper, the design result of objective I is given as an example. Optical path of objective I is shown in Figure 3c, a folding mirror is added to reduce the total length, and the image plane is led to the back of the system to facilitate the docking with spectrometers. MTF curves of objective I are shown in Figure 3d. In the wavelength range of 0.3–1.01 μm , the imaging quality is close to the diffraction limit, and its MTF value is above 0.77 at the Nyquist frequency. Its grid distortion is 0.29%. In addition, the objective is designed to be telecentric to match the pupil of spectrometers. At the objective's entrance pupil, light is scanned in a time-sharing manner to cover the FOV of $10.24^\circ \times 10.24^\circ$. Therefore, the scanning angle of the scanning mirror is $5.12^\circ (\pm 2.56^\circ)$, corresponding to the FOV of $0.64^\circ (\pm 0.32^\circ)$ for GeoFWHIS.

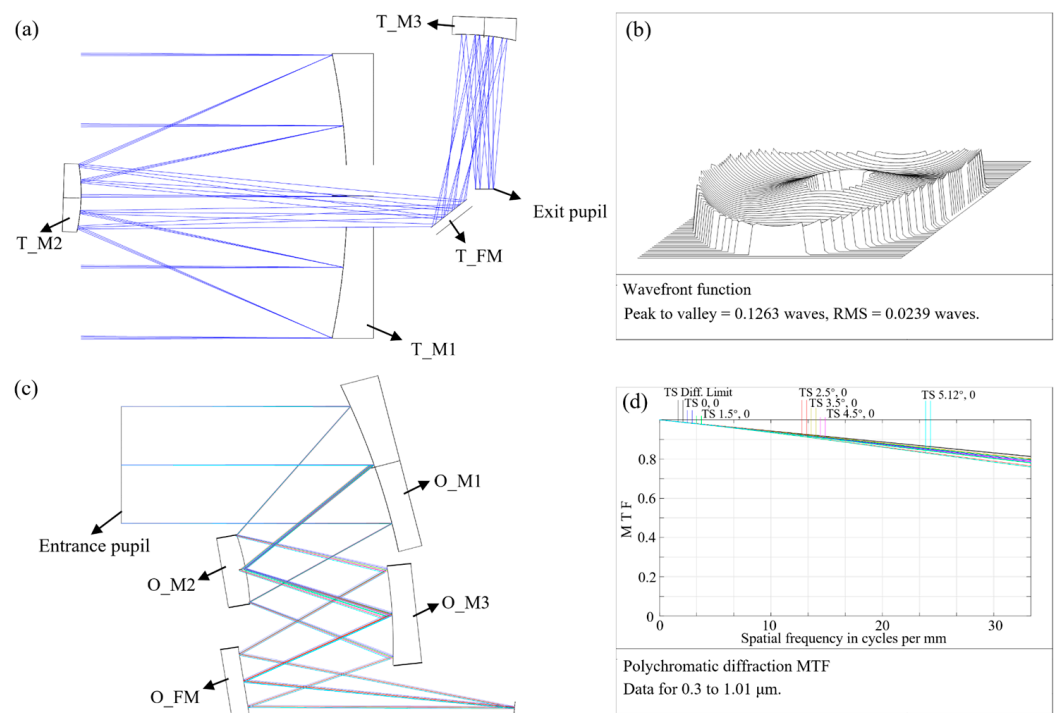


Figure 3. (a) Optical path of the afocal telescope and (b) its wavefront map. (c) Optical path of objective I and its (d) MTF curves.

3.2. High-Fidelity Spectrometers

The spectrometer is one of the most important parts of GeoFWHIS. In each band, four identical spectrometers are spliced to cover the image plane of the fore-optics completely. The slit of a single spectrometer is still quite long, especially in B1 and B2 bands, with a maximum slit length of 61.44 mm. The splicing diagram of four spectrometers is shown in Figure 4, and the slits of two adjacent spectrometers have some overlap. The total length of the spliced slit L , the single slit length S , and the overlap δ_S have the following relationship:

$$L = 4S - 3\delta_S \quad (1)$$

To avoid the interference of two adjacent spectrometers at the same side, the spectrometer width W needs to satisfy the following inequality, which requires the spectrometer to have a small volume while having a long slit.

$$W < 2S - 2\delta_S \quad (2)$$

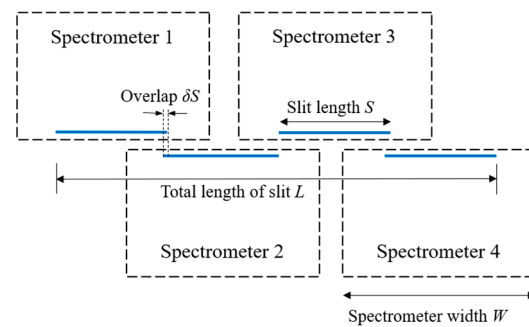


Figure 4. Slicing of spectrometers.

Besides the compact size, high-fidelity [39,40] performance is also critical to spectrometers, and it is essential to realize quantitative hyperspectral remote sensing. The fidelity of a spectrometer is affected by many properties, such as MTF, spectral response function (SRF), spectral distortions (smile and keystone), stray light, SNR, etc. Various spectrometer configurations suitable for long slit have been reported, as shown in Figure 5. Including Offner configuration [41], Wynne–Offner configuration [42,43], freeform Offner configuration [44], immersed Offner configuration [45], Dyson configuration [46], Wynne–Dyson configuration [47], R-T configuration [25], the catadioptric system [48], and CCVIS [23] proposed by Chrisp. These configurations have excellent spectral imaging performance in specific scenes, but not all of them are compact, high-fidelity, and fit for splicing. We designed these configurations to have the same wavelength range (0.55–1.01 μm) but different slit lengths and F numbers. The various configurations are arranged in Figure 5 according to their normalized volume V . Optical performance, including wavefront error (WFE) and spectral distortions of these configurations, are shown in Table 3, and λ is 632.8 nm in this table.

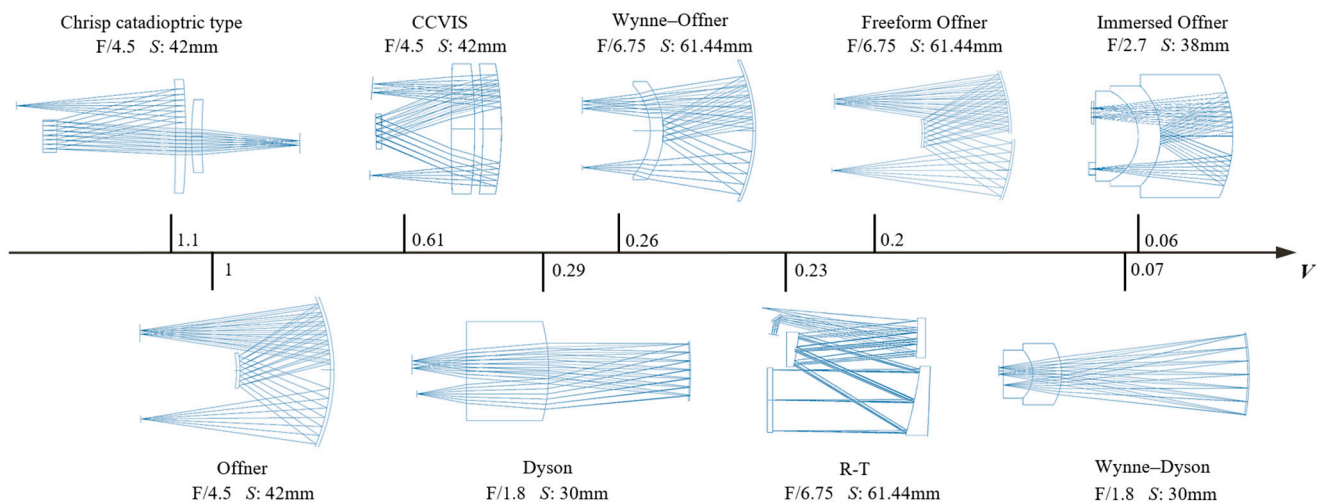


Figure 5. Optical path diagrams of different configurations and their volume.

Characteristics of different configurations are also compared in Table 3. The Wynne–Dyson and immersed Offner types have the smallest volume, only about 1/15 of the classic Offner type. However, the Wynne–Dyson configuration is unsuitable for splicing because of its short working distance and a small clearance between the slit and image plane. The immersed Offner configuration can be used for splicing, and we manufactured it in our previous work to solve the contradiction between large relative aperture, long slit, and small volume [45]. However, it has high cost and risk in the development process, mainly suitable for the system with large relative aperture. The R-T configuration and the freeform Offner configuration also have relatively compact structures. However, the double-pass aspheric mirrors and freeform elements are challenging and costly to manufacture. Since spectrometers in GeoFWHIS have small relative apertures, the spectrometers in B1, B2, and

B3 bands are designed with Wynne–Offner configuration, and the spectrometers in B4 and B5 bands are designed with classic Offner configuration. There has been much research on the aberration theory and design methods of the Offner spectrometer [12,49], and the authors have also made detailed analyses of the Wynne–Offner spectrometer in previous work [43,50]. The designed spectrometers for five bands are shown in Figure 6, and their characteristics are shown in Table 4. There are two slits in B3 and B4 spectrometers because the detectors of B3 and B4 bands are made up of two chips with 1024×256 pixels. The double slit assembly is shown in Figure 12c.

Table 3. Optical performance of the designed spectrometers and comparison of their characteristics.

Spectrometer Types	WFE/ λ	Smile/ μm	Keystone/ μm	V	Characteristics
Offner	0.10	0.12	0.09	1	<ul style="list-style-type: none"> • long working distance • large volume with long slit
Wynne–Offner	0.04	0.02	0.07	0.26	<ul style="list-style-type: none"> • compact with long slit • anastigmatic
Freeform Offner	0.07	0.08	0.15	0.2	<ul style="list-style-type: none"> • compact with long slit • extremely difficulty • high cost
Immersed Offner	0.03	0.03	0.08	0.06	<ul style="list-style-type: none"> • ultra-compact • large relative aperture • short working distance
Dyson	0.18	0.35	0.22	0.29	<ul style="list-style-type: none"> • short working distance • large relative aperture • short slit
Wynne–Dyson	0.06	0.12	0.10	0.07	<ul style="list-style-type: none"> • ultra-compact • small slit-to-image space • long slit
R-T	0.09	1.55	1.03	0.23	<ul style="list-style-type: none"> • compact with long slit • tight tolerance • small slit-to-image space • residual distortions
Chrip catadioptric type	0.24	2.20	2.35	1.1	<ul style="list-style-type: none"> • long working distance • residual aberration
CCVIS	0.11	0.34	0.25	0.61	<ul style="list-style-type: none"> • long working distance • large volume with long slit

It can be seen from Table 4 that the MTF values of spectrometers at the Nyquist frequency are close to the diffraction limit. The smile and keystone are both spectral distortions of the spectrometer, which will affect the spectral and spatial uniformity, respectively. Spectral uniformity demands that the monochromatic image of the slit at any wavelength be straight [40]. Smile is the deviation of monochromatic slit image from a straight line, as

shown in Figure 7a. Spatial uniformity demands that the magnification of the spectrometer be independent of wavelength so that the monochromatic slit images are of the same length at any wavelength. Deviation from this condition is often referred to as ‘keystone’, as shown in Figure 7b. The smile and keystone requirements for the GeoFWHIS spectrometers are both less than 10% of a pixel. Moreover, in addition to reducing smile and keystone in optical design, the spectral uniformity requires the slit image to be aligned with the detector array, and the spatial uniformity requires the dispersion line of any field point be aligned with the detector array. This requires high alignment accuracy of the spectrometer and detector, which will be discussed in Section 4.2. In this section, we evaluate the smile and keystone, as shown in Table 4; both of them are less than 1% of a pixel in each band, indicating extremely low spectral distortions.

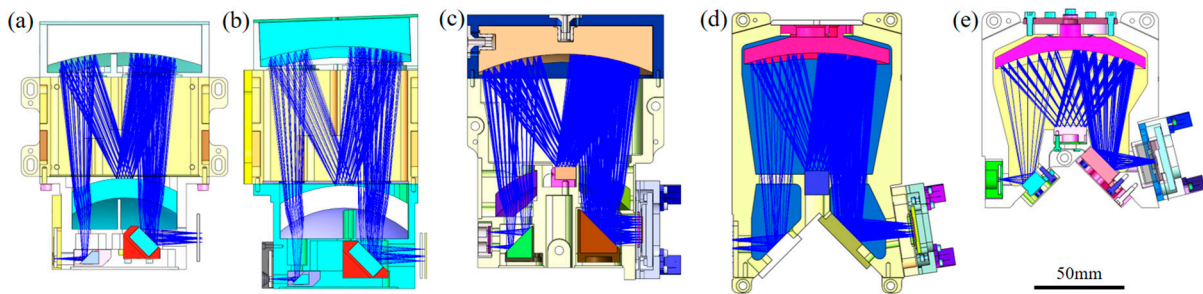


Figure 6. Profile map of spectrometers in GeoFWHIS. (a–e) from B1 band to B5 band.

Table 4. System parameters and performance of spectrometers.

Bands	B1	B2	B3	B4	B5
MTF	0.86	0.77	0.72	0.41	0.28
Smile/pixel	0.06%	0.11%	0.26%	0.31%	0.95%
Keystone/pixel	0.33%	0.47%	0.79%	0.42%	1.00%
Size/mm	140 × 110 × 100	170 × 111 × 106	160 × 132 × 89	168 × 165 × 88	90 × 92 × 49

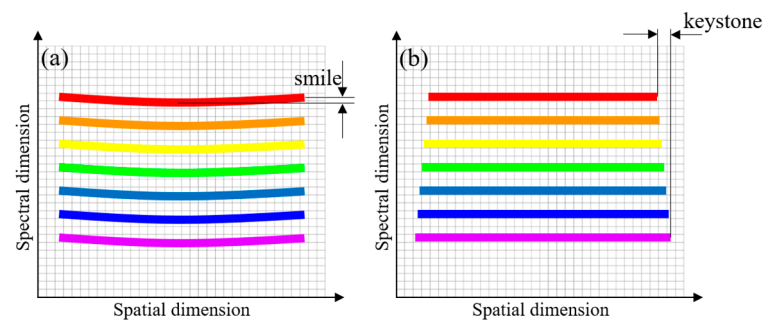


Figure 7. Spectral lines showing smile and keystone distortions. (a) Smile, (b) keystone.

The spectral response function (SRF) [39] and the spectral full field display (SFFD) [51] of B1 and B3 bands are given in Figure 8. SRF describes the response of the spectrometer to the monochromatic light with unit intensity, and it is affected by the spectrometer optical system and the detector sampling. We consider that the slit is along the x -axis, and then the spectral direction is along the y -axis. If the detector sampling is not taken into account, SRF of the optical system—i.e., SRF_{opt} —can be computed as the convolution of the slit function (a rectangular function of width y_s , y_s the slit width) and the y -line spread function (LSF) of the optical system. If the detector sampling is taken into account, SRF of the instrument—i.e., SRF_{ins} —can be computed as the convolution of the SRF_{opt} and the detector sampling function (a rectangular function of width y_d , y_d the sampling width).

$$SRF_{opt} = \text{rect}(y_s) * LSF(y) \quad (3)$$

$$SRFF_{ins} = \text{rect}(y_s) * LSF(y) * \text{rect}(y_d) \quad (4)$$

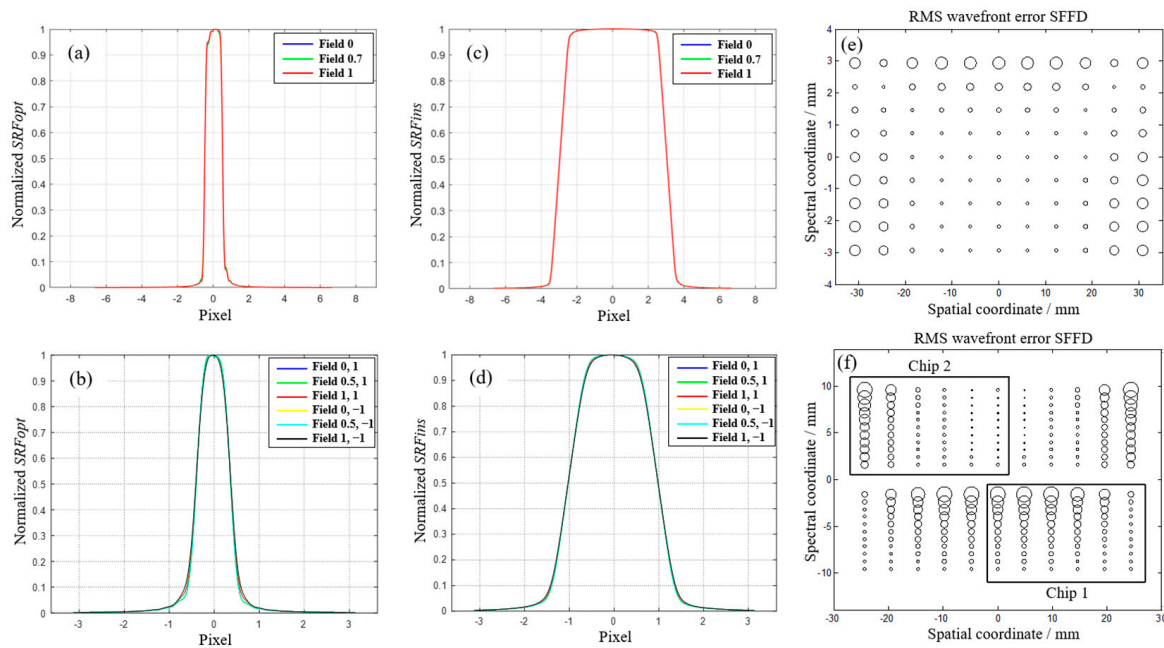


Figure 8. (a) SRF_{opt} of B1 at $0.43 \mu\text{m}$; (b) SRF_{ins} of B1 at $0.43 \mu\text{m}$, detector samples with $6 \times$ pixels (pixel size $15 \mu\text{m}$) binning; (c) SRF_{opt} of B3 at $1.75 \mu\text{m}$; (d) SRF_{ins} of B3 at $1.75 \mu\text{m}$, detector samples with $2 \times$ pixels (pixel size $32 \mu\text{m}$) binning; (e,f) SFFDs of B1 and B3 spectrometers.

Figure 8a,b show the SRF_{opt} of B1 and B3 spectrometers at the middle wavelength of the band, respectively. Figure 8c,d show SRF_{ins} of B1 and B3 spectrometers with pixel-binning sampling, respectively. A high-fidelity spectrometer shall have uniform SRFs at different fields. It can be seen from the curves in Figure 8a–d that the SRFs at different fields coincide well. The full width at half maximum (FWHM) of SRF_{opt} accounts for 1 pixel (pixel size $15 \mu\text{m}$) in B1 band and 0.75 pixel (pixel size $32 \mu\text{m}$) in B3 band. The FWHM of SRF_{ins} accounts for 6 pixels in the B1 band and 2 pixels in the B3 band.

SFFD displays the aberration distribution of the image plane by traversing the aberrations of multiple sampling points in spatial and spectral dimensions. Figure 8e,f show the SFFD of wavefront error of B1 and B3 spectrometers, respectively. The size of each circle represents the wavefront error at the corresponding position in the image plane. The aberration distribution in the spectral plane is uniform without drastic change. The maximum wavefront error is only 0.031λ in the B1 band and 0.035λ in the B3 band, close to the diffraction limit.

Low stray light is another important property for realizing high-fidelity spectral imaging. We design multiple baffles to reduce stray light, as shown in Figure 9a, mainly to eliminate the reflected light from meniscus surface and the diffraction light in non-working orders. Using non-sequential ray tracing, the stray light coefficients of the spectrometer in spatial dimension and spectral dimension are analyzed, respectively. The simulated illuminance of the image plane is shown in Figure 9b–d. Figure 9c shows the illuminance map when the slit is blocked by 10%, and the average illuminance at the center of the blocked portion is I_{spa} . Figure 9d shows the illuminance map when the wavelength range is notched by 10%, and the average illuminance at the center of the notched portion is I_{spe} . The stray light coefficient in spatial dimension S_{spa} and in spectral dimension S_{spe} can be calculated by the following equations.

$$S_{spa} = \frac{I_{spa}}{I_{nor}} \quad (5)$$

$$S_{spe} = \frac{I_{spe}}{I_{nor}} \quad (6)$$

where I_{nor} is the average illuminance at the center of the image plane in Figure 9b. The analysis results show that the stray light coefficients are pretty small in the B1 band, only 0.05% in the spatial dimension, and 0.09% in the spectral dimension.

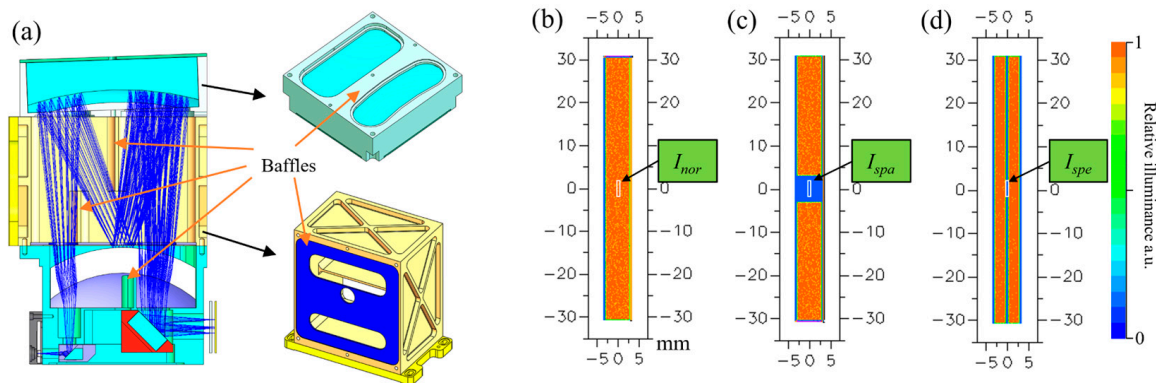


Figure 9. (a) Optical–mechanical model of B1 spectrometer and (b–d) illuminance maps of the image plane. (b) shows the illuminance map of the spectrometer’s image plane, (c) shows the illuminance map when the slit is blocked by 10%, and (d) shows the illuminance map when the wavelength range is notched by 10%.

3.3. Optical System of GeoFWHIS

Design results and performance of each component of GeoFWHIS have been aforementioned. In this section, the optical system of GeoFWHIS is given, and its optical path diagram is shown in Figure 10. To evaluate its imaging performance adequately, MTF curves of each spectrometer in each band are shown in Figure 11. The columns (a) to (d) correspond to spectrometer 1–4 in Figure 4. We can see that the MTF values of spectrometers 2 and 3 are slightly higher than those of spectrometers 1 and 4. This is because the image quality of the fore-optics in the central field of view is better than that of the edge field of view, and the spectrometers 1 and 4 are aligned on both sides of the slit image of the fore-optics. The lowest MTF values at Nyquist frequency of B1 to B5 bands are 0.59, 0.48, 0.59, 0.39, and 0.25, respectively. They are high enough to meet the requirements in Table 1, which are 0.17, 0.17, 0.17, 0.12, and 0.12, respectively.

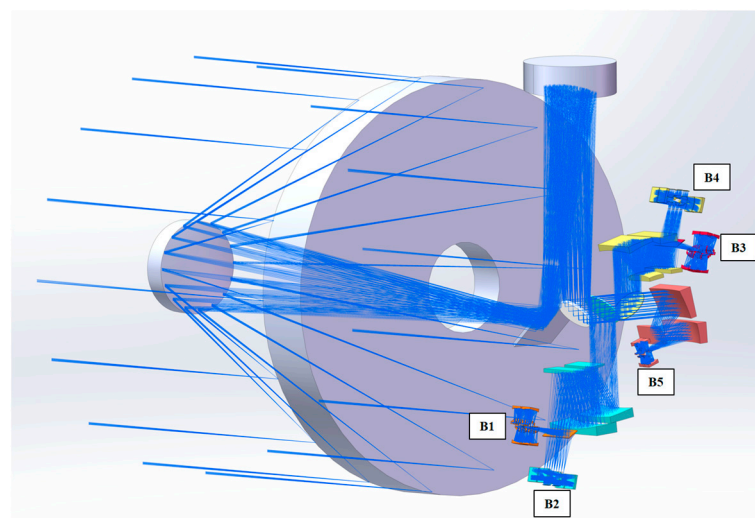


Figure 10. Optical path diagram of GeoFWHIS.

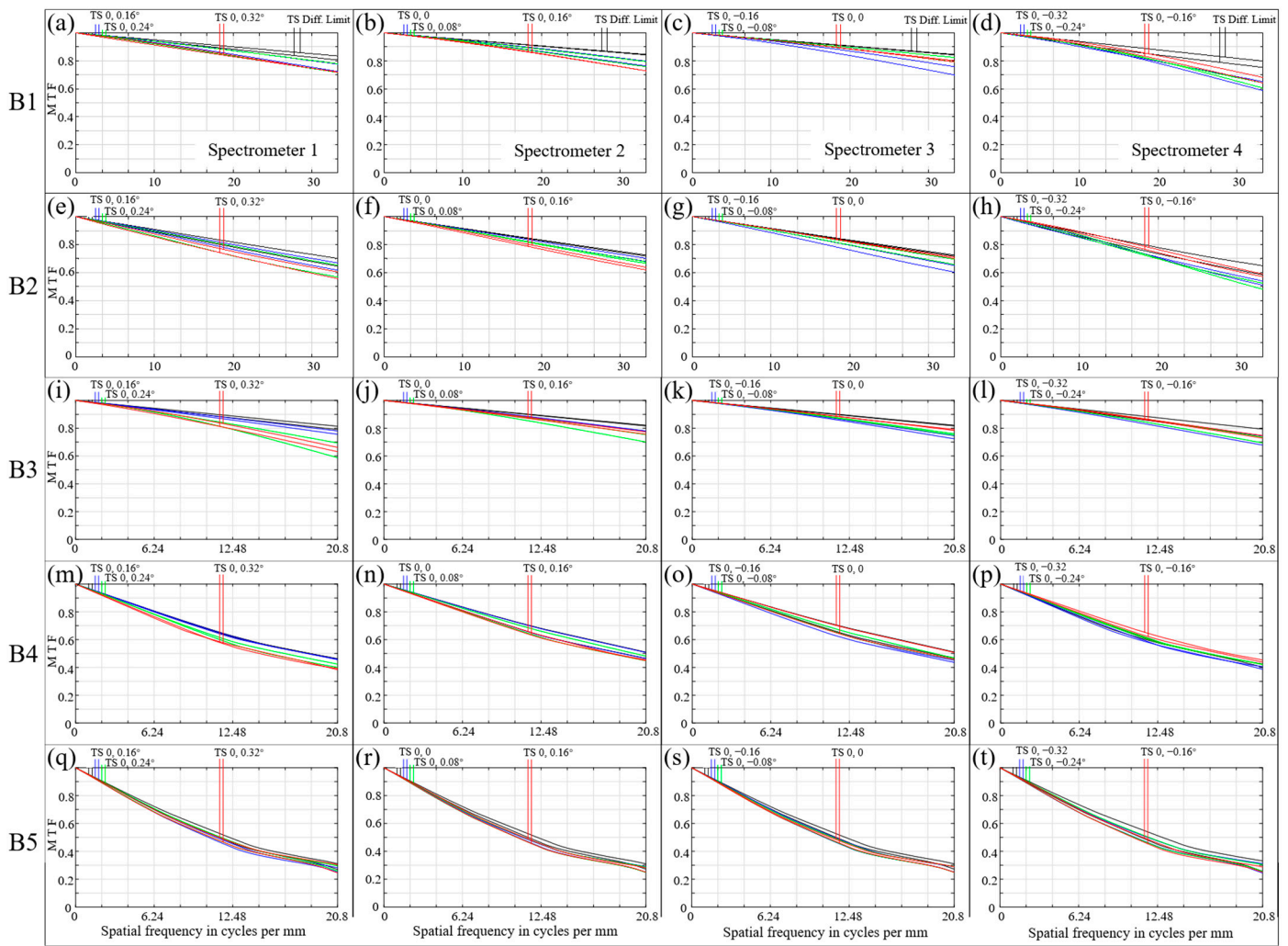


Figure 11. MTF curves of GeoFWHIS. (a–d) for 4× B1 spectrometers at 0.43 μm , (e–h) for 4× B2 spectrometers at 0.78 μm , (i–l) for 4× B3 spectrometers at 1.75 μm , (m–p) for 4× B4 spectrometers at 4 μm , (q–t) for 4× B5 spectrometers at 10.25 μm .

4. Experiment Results

4.1. Manufacture of Slits and Gratings

Slits and gratings are core components of the spectrometers in GeoFWHIS, and their performance directly affects the spectral quality of the system. The slit is the field stop of a spectrometer, and its geometrical error and edge defect will decrease the spectral resolution, distortion, and uniformity. Slits in GeoFWHIS are long and narrow, especially in B1 and B2 bands; the length of a single slit is 61.44 mm, but the width is only 15 μm , and the length ratio to width is more than 4000. It is quite challenging to ensure the slit edge's straightness, parallelism, and uniformity by traditional methods such as manual grinding, mechanical scribing, and laser processing. In this paper, long slits based on silicon substrate are manufactured by semiconductor technology [50], as shown in Figure 12. The geometric error of the slit can be strictly controlled by stepping lithography technology. Figure 12b is the micrograph of the slit in the B1 band. Its edge is straight and sharp without noticeable burr within the whole slit range. The measured width is 14.99 μm , and the parallelism error of two edges is less than 0.5 μm .

Convex blazed grating is the aperture stop of the spectrometer. Its groove density, shape, diffraction efficiency, and surface error will directly affect the spectrometer's transmittance, stray light, and wavefront error. Diffraction gratings of the spectrometers in GeoFWHIS have low groove density and small blazed angles. Especially in the B5 band,

the groove density is only 8.8 lp/mm, and the blazed angle is less than 3° . It is difficult to etch sawtooth grooves with large periods and small blazed angles on a convex substrate by ion beam etching. In this paper, we jointly design the optical system and manufacturing process to optimize the grating groove suitable for current precision micro-nano processing. The manufactured gratings and their theoretical and measured diffraction efficiencies are shown in Figure 13. The vertex angle slightly deviates from the ideal right angle, being an obtuse or rounded angle. This deviation will decrease the peak efficiency of the grating. The peak efficiencies of each band are still more than 70%, which fully ensures the transmittance and SNR of the spectrometer, and the highest peak efficiency is 86.4% in the B4 band.

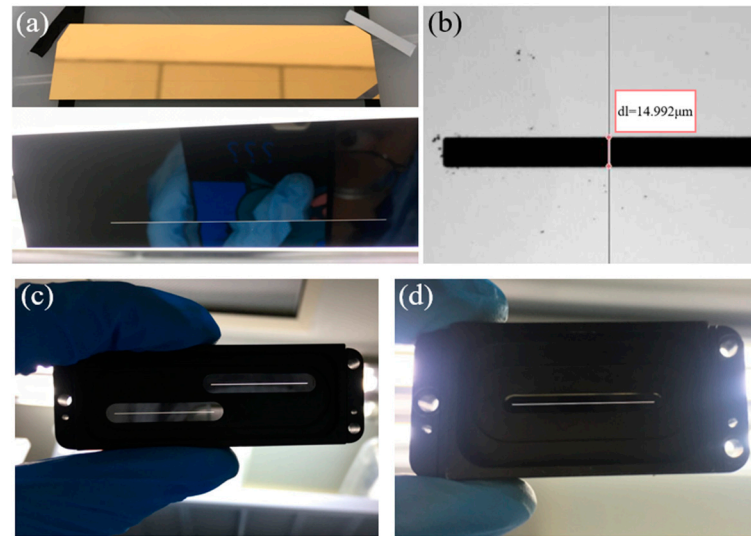


Figure 12. Slits based on silicon. (a) B1 and B2 slits, (b) $10\times$ micrograph of B1 slit, (c) B3 and B4 slits, (d) B5 slit.

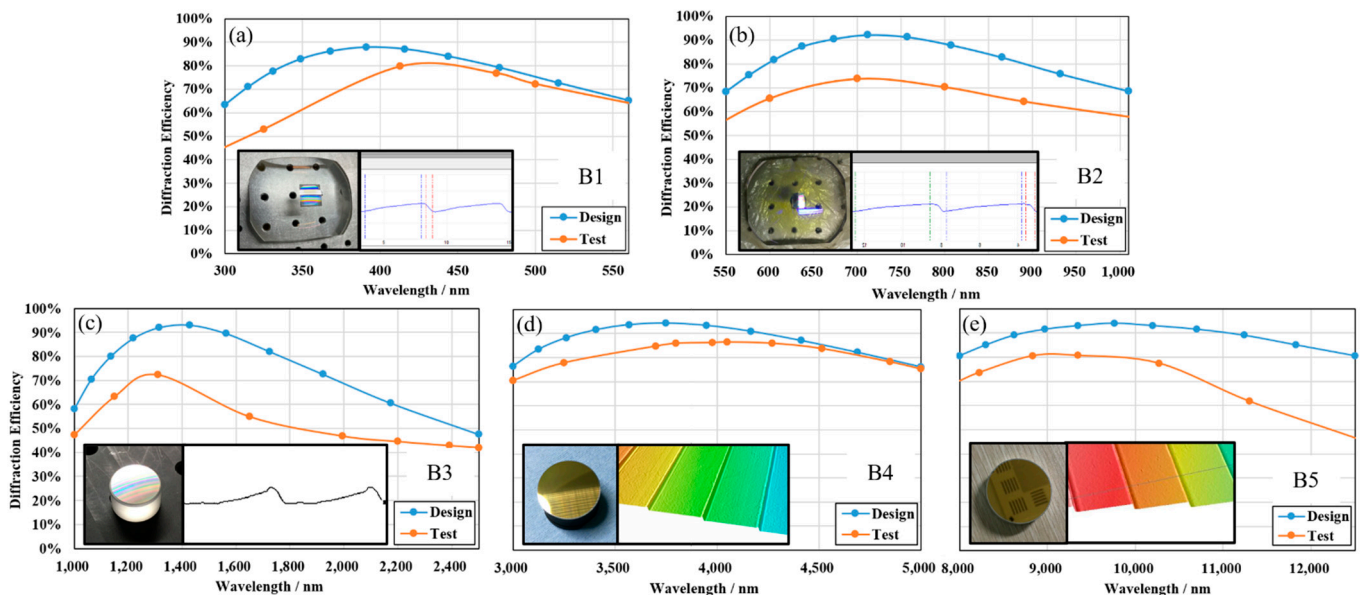


Figure 13. Convex blazed gratings and their groove shapes and diffraction efficiencies. (a) B1 band, groove density 312.1 lp/mm, blazed angle 3.8° ; (b) B2 band, groove density 210.1 lp/mm, blazed angle 4.75° ; (c) B3 band, groove density 68.5 lp/mm, blazed angle 3.1° ; (d) B4 band, groove density 19.1 lp/mm, blazed angle 2.8° ; (e) B5 band, groove density 8.8 lp/mm, blazed angle 2.8° .

4.2. Alignment

Usually, Offner and Wynne–Offner spectrometers have a loose alignment tolerance when the MTF is used as a criterion. However, the concentricity of convex grating and concave mirror is quite sensitive to spectral distortions. In the long-slit spectrometer presented in this paper, the concentricity error is rigorous, which must be controlled below 0.01 mm to keep the smile and keystone at less than 10% of a pixel. To realize the high-precision alignment of spectrometers, we developed a high-precision point-source microscope, as shown in Figure 14a. It is used to find spherical centers of optical surfaces to assist the alignment of spectrometers, with a lateral accuracy of 0.4 μm and an axial accuracy of 1.0 μm . In B1 and B2 bands, it is used to determine the relative position of the meniscus-grating and the concave mirror, as shown in Figure 14b. In the B3 band, it is used to determine the relative position of two separate menisci, the convex grating, and the concave mirror. The experiment device for adjusting the separate menisci is shown in Figure 14c,d shows the image of two spherical centers after alignment, with an interval of 3.6 μm . After aligning the convex grating and the concave mirror, we aligned the slit. The slit is required to be aligned parallel to the grating groove, so that a uniform spectral image can be obtained; that is, the polychromatic image of any field point should form a dispersion line that is straight and perpendicular to the slit, which is aligned with the detector array. The slit-to-grating rotation is adjusted by monitoring the spectral lines' arrangement while the slit is illuminated by a mercury–cadmium (Hg–Cd) lamp. Figure 15 shows the spectral lines in the image plane when the slit-to-grating rotation is or is not corrected.

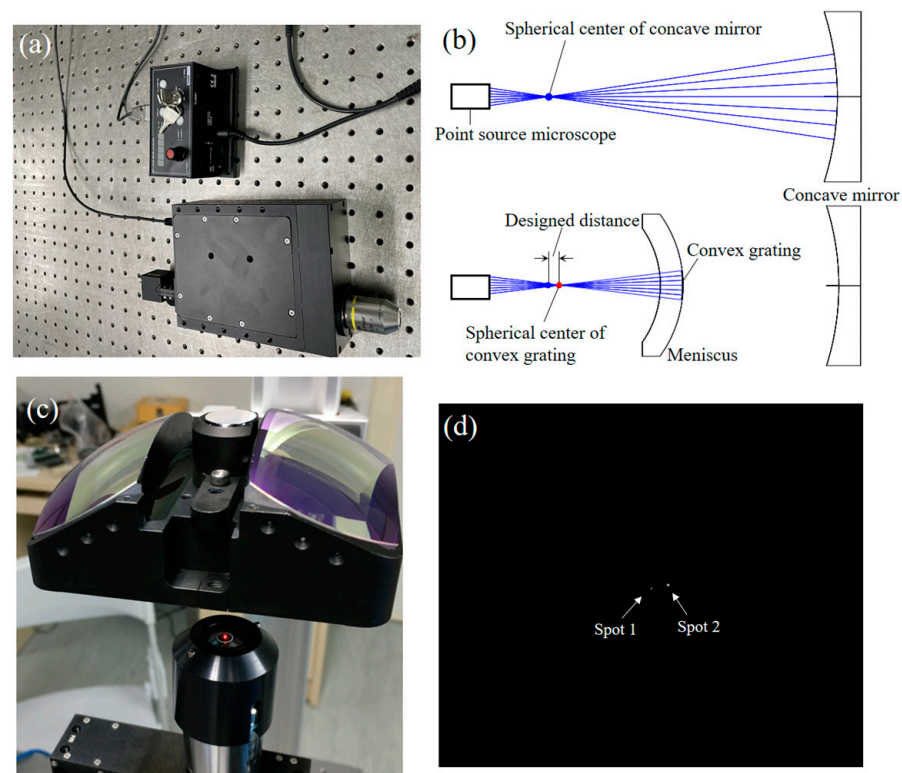


Figure 14. Alignment of spectrometers by utilizing a point source microscope. (a) Self-developed point-source microscope, (b) alignment of meniscus-grating and concave mirror in B1 and B2 spectrometers, (c) alignment of two separated menisci in B3 spectrometer with point-source microscope, (d) star images of two spherical surfaces in the field of the point source microscope.

The B4 and B5 spectrometers are designed in a snap-together manner [52,53] with an all-metal structure to minimize the elements and simplify the alignment process. These two spectrometers can achieve high performance only by assembling without adjusting. The prototypes of spectrometers for each band are shown in Figure 16.

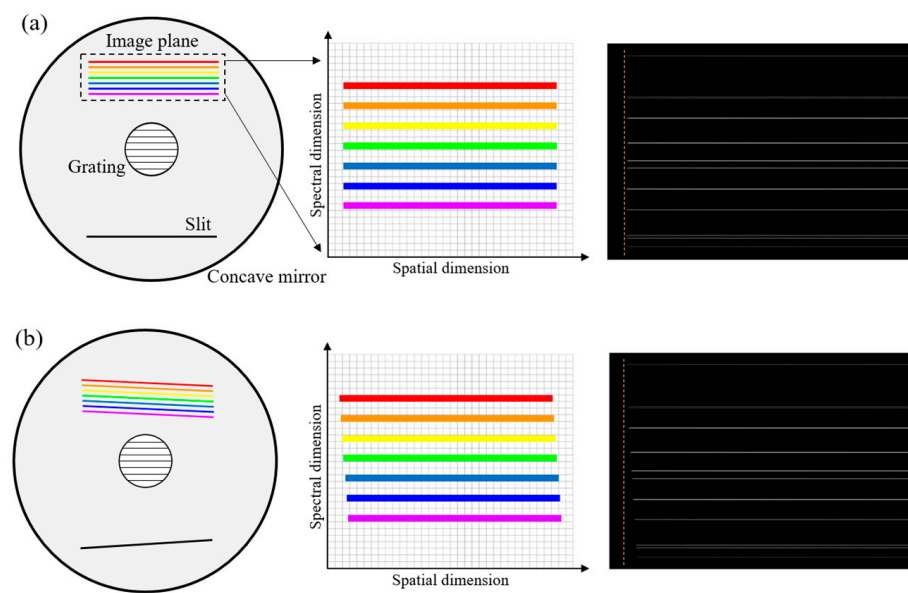


Figure 15. Slit-to-grating rotation affects the spatial uniformity of spectral image. The slit is parallel to the grating groove in (a), and the dispersion direction is perpendicular to the monochromatic slit images. The slit rotates an angle relative to the grating groove in (b), and the dispersion direction is not perpendicular to the monochromatic slit images.

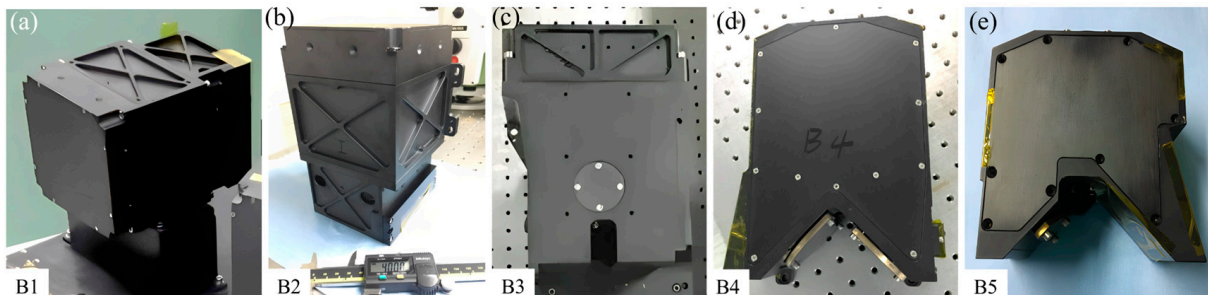


Figure 16. Spectrometers of five sub-bands. (a–e) for spectrometers of B1–B5.

4.3. Test of Spectrometers

We take the test results from B1, B3, and B5 spectrometers as examples. The device for testing the spectral performance of the B1 spectrometer is shown in Figure 17a,b. A Hg–Cd lamp is used to illuminate the slit, and a small-pixel CCD detector with a pixel size of $5.5 \mu\text{m}$ is used to acquire the spectral lines of the lamp. The measured spectral lines are shown in Figure 17c. There are abundant spectral lines of 546.1 nm, 508.5 nm, 479.9 nm, 467.8 nm, 435.8 nm, 404.6 nm, 365.0 nm, 346.3 nm, and 312.9 nm within the B1 wavelength range (300–560 nm). By calculating the centroid coordinates of these spectral lines in spectral dimension, it can be obtained that the dispersion power of the B1 spectrometer is 44.1 nm/mm . Pixel size of the detector used in the B1 spectrometer is $15 \mu\text{m}$, and the spectral sampling distance with $6 \times$ pixels binning is 3.97 nm , consistent with the design. SRFs of the spectrometer are shown in Figure 17d, the SRF_{opt} is fitted from raw data, and the SRF_{ins} is the SRF after $6 \times$ pixels binning. The spectral resolution is the full width at half maximum (FWHM) of SRF_{ins} . Table 5 gives the spectral resolution at different fields and wavelengths of the B1 spectrometer. It can be seen that the spectral resolution in the whole image plane is uniform.

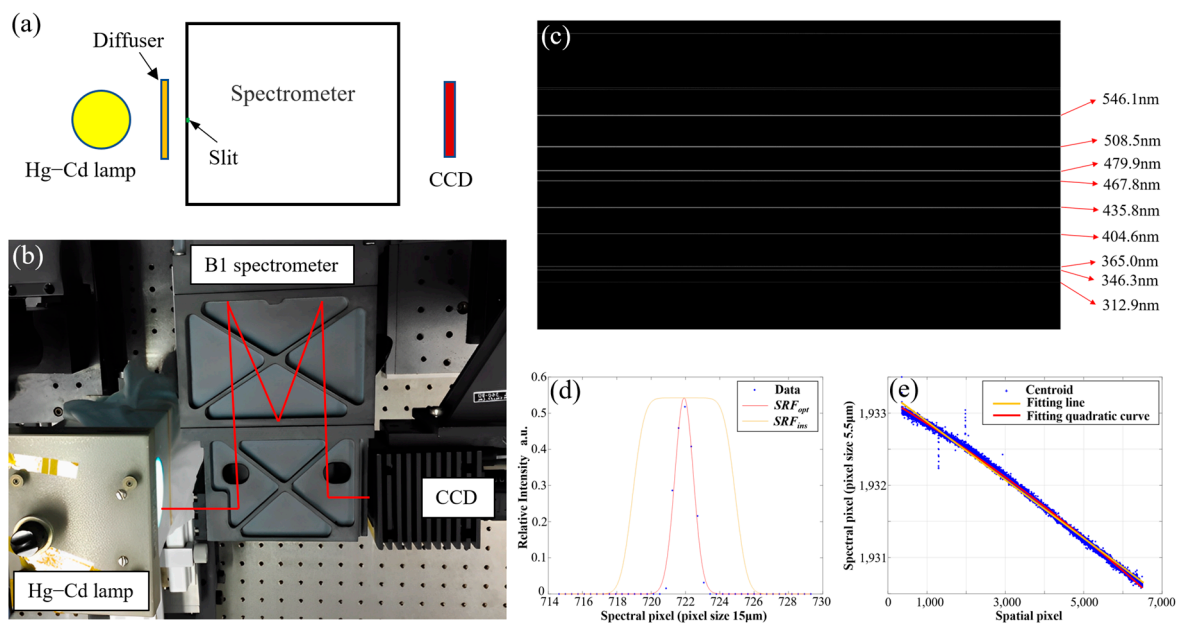


Figure 17. (a,b) Test device and (c–e) test results from the B1 spectrometer. (c) Spectral lines of the Hg–Cd lamp, (d) SRFs from the 479.9 nm spectral line; the SRF_{opt} is fitted from raw data, and the SRF_{ins} is the SRF after $6 \times$ pixels binning. (e) Scatter diagram of the 479.9 nm spectral line and its fitting curve.

Table 5. Spectral resolution of B1 spectrometer with $6 \times$ pixels binning.

Wavelength/nm	FWHM of SRF at Different Fields/nm					Average
	−1 Field	−0.5 Field	0 Field	+0.5 Field	+1 Field	
312.9	3.92	3.93	3.93	3.92	3.93	3.95
346.3	3.98	3.97	3.95	3.97	3.96	3.98
404.6	4.02	3.98	3.99	4.00	4.00	4.01
435.8	4.01	4.02	4.01	4.00	4.02	4.02
467.8	3.99	3.98	3.98	3.98	4.00	4.00
479.9	4.02	4.01	4.01	4.00	4.02	4.02
508.5	4.01	4.02	4.01	4.00	4.01	4.01
546.1	4.01	4.02	4.00	3.99	4.00	4.00

Smile distortion in this paper is defined as the deviation of monochromatic slit image from a straight line, and it is one of the factors that affect the spectral uniformity. We use a small-pixel detector to measure the smile in order to improve the accuracy. In fact, rotation of the detector with respect to the slit will affect the test results, for that it will cause the linear shift in wavelength at different spatial channels in a detector row. However, it should be clear that the detector-to-slit rotation is not an optical characteristic, and it is caused by the installation of the detector. Therefore, when we test the spectrometer’s smile with a detector that is not used for practical work, we need to exclude the detector rotation in the test process. Figure 17e shows the scatter diagram of 479.9 nm spectral line. It is obviously not parallel to the spatial coordinate axis, and has a tilt of about 2.5 pixels (pixel size $5.5 \mu\text{m}$) in the spectral direction. This slope is caused by the incomplete alignment of the spectral lines and the detector array during the test. That means the detector-to-slit rotation and the slope cannot be directly accounted for as the spectrometer’s smile. By fitting a spectral line to a straight line and a curve, as shown in Figure 17e, the smile distortion can be calculated as the peak–valley value of the distance between the fitting curve and the fitting straight line. The smile at 479.9 nm is the largest, accounting for 1.6% of a pixel (pixel size $15 \mu\text{m}$). This value is the test result after excluding the detector-to-slit rotation. It

is shown that the spectrometer optical system has extremely small smile, and the later installation of the detector also require high alignment accuracy to minimize the spectral non-uniformity as much as possible, and the detector alignment must also enter in the final system assessment.

Keystone distortion in this paper is defined as the difference in the slit images' lengths at different wavelengths. Figure 18a shows the schematic diagram of the device for testing the keystone. A broadband polychromatic point source is formed at both ends of the slit, and two dispersion lines are formed at the image plane, as shown in Figure 18b. The keystone can be calculated by the slope difference of the dispersion lines:

$$\text{Keystone} = (k_1 - k_2)d_{\text{dispersion}} \quad (7)$$

where k_1 and k_2 are the slope of dispersion line 1 and 2, respectively. $d_{\text{dispersion}}$ is the dispersion width of the spectrometer, which is $5.90 \mu\text{m}$ for the developed B1 spectrometer. The experiment device is shown in Figure 18c, and the dispersion lines collected by CCD are shown in Figure 18d. The test result shows that the keystone of the B1 spectrometer is 1.9% of a pixel (pixel size $15 \mu\text{m}$).

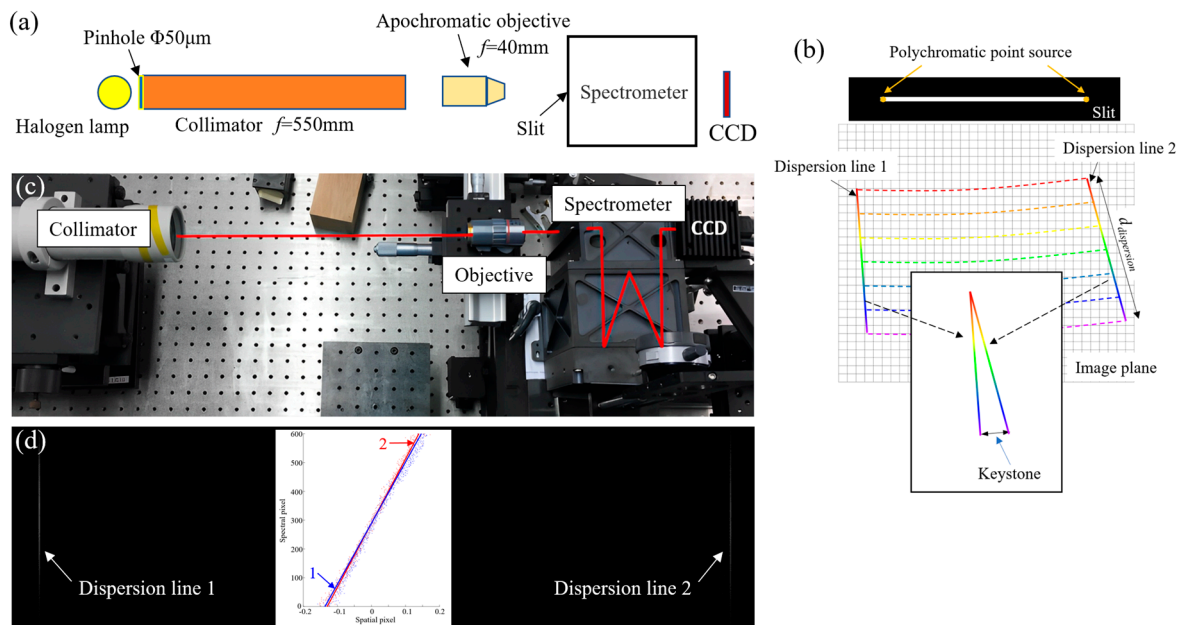


Figure 18. Test of keystone. (a) Schematic diagram of the test device, (b) the polychromatic point source is formed at both ends of the slit, and two dispersion lines are formed at the image plane, (c) the experiment device, and (d) dispersion lines corresponding to both ends of the slit.

In Figure 18d, the dispersion lines have a slope of about 0.3 pixels (pixel size $5.5 \mu\text{m}$), and this is caused by the incomplete alignment of the dispersion lines and the detector array during the test. That means the detector-to-grating rotation. The tested keystone calculated by Equation (7) not only excludes the effect of detector-to-grating rotation, but also ignores the slit-to-grating rotation. When we test the optical performance of spectrometer, we need to exclude the effect of the detector-to-slit and detector-to-grating rotation, but the slit-to-grating rotation could also cause spatial non-uniformity, as described in Section 4.2. Therefore, the perpendicularity of the spectral dimension and the spatial dimension needs to be measured. In the process of testing smile and keystone, as shown in Figures 17b and 18c, we only changed the light source illuminating the slit, and the relative position of CCD and spectrometer is unchanged. Thus, we can use the spectral lines and dispersion lines acquired in two experiments to calculate the angle between the spatial dimension and the spectral dimension. The average angle between the spectral lines in Figure 17c and the dispersion lines in Figure 18d is 89.98° , indicating extremely high rotational alignment

accuracy of the slit and grating. Such a high perpendicularity only results in a spatial alignment error of $2\ \mu\text{m}$ ($d_{\text{dispersion}} \times \tan 0.02^\circ$) at most between the dispersion line and the detector array.

Meanwhile, the MTF of the B1 spectrometer is tested by the OPTIKOS[®] lens measurement system, including a long-focus collimator, a microscope, and a computer containing processing software, as shown in Figure 19a. An optical filter can be added in front of the light source of the collimator to obtain near-monochromatic parallel light. We use a Mitutoyo[®] 10× apochromatic objective in the parallel light to form a point source at the slit of the spectrometer. The OPTIKOS[®] lens measurement system captures the spot image of the optical system under test through a microscope to obtain its point spread function (PSF), and then performs Fourier transform on PSF to obtain the MTF of the optical system. However, the near-monochromatic point source forms a slender image instead of a spot image after passing through the spectrometer and is then captured by the microscope, as shown in Figure 19b. Only the PSF in the spatial dimension can be obtained; thus, only the spatial MTF can be tested in such a configuration. The tested MTF curve is shown in Figure 19c, and the MTF value is 0.81 at 460 nm and 33.3 lp/mm, close to the diffraction limit. In spectral dimension, we generally use the SRF to show its spectral performance, which has been discussed above.

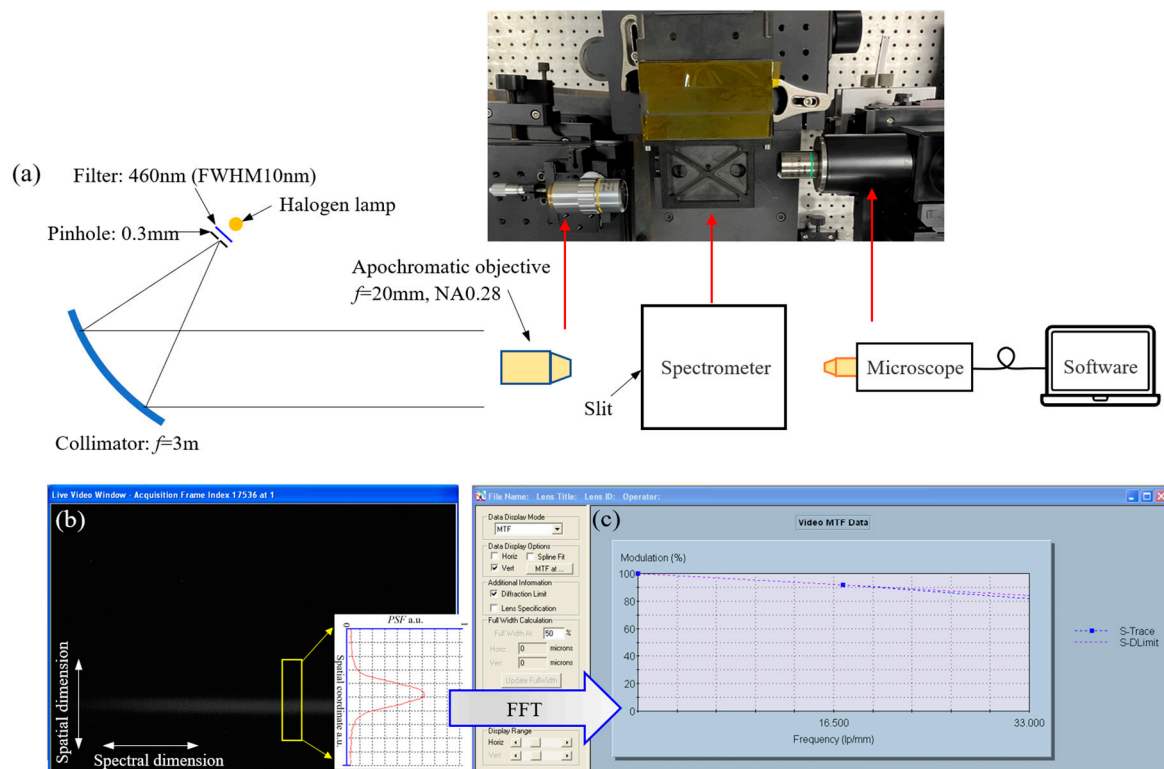


Figure 19. Test of MTF. (a) Schematic diagram of the test device and the experiment device, (b) the narrow band point light source with the center wavelength of 460 nm forms a slender image after passing through the spectrometer and is captured by the microscope, (c) the MTF curve.

In addition, stray light of the B1 spectrometer is also tested using a large diameter integrating sphere, as shown in Figure 20a. To test the stray light more accurately, we use a neutral density (ND) filter to artificially extend the dynamic range of the detector. We first increase the brightness of the integrating sphere to saturate the detector on the image plane of the spectrometer. Secondly, we place a ND filter with an optical density of 1 in front of the slit, and the detector acquires a uniform dispersion image, as shown in Figure 20b, and its average grey level is I'_{nor} . Then, we remove the ND filter and install a block in front of the slit. The average grey level at the center of the blocked portion in the image is I'_{spa} , as

shown in Figure 20c. Next, we remove the block and place a notch filter in front of the slit. The average grey level at the center of the notched portion in the image is I'_{spe} , as shown in Figure 20d. The spatial stray light coefficient S'_{spa} and the spectral stray light coefficient S'_{spe} can be calculated by the following equations.

$$S'_{spa} = \frac{I'_{spa} - I'_{bac}}{(I'_{nor} - I'_{bac}) / T_{ND}} \quad (8)$$

$$S'_{spe} = \frac{I'_{spe} - I'_{bac}}{(I'_{nor} - I'_{bac}) / T_{ND}} \quad (9)$$

where I'_{bac} is the background grey level of the detector, and T_{ND} is the transmission of the ND filter. The test results show that the stray light coefficient is only 0.22% in spatial dimension and 0.45% in spectral dimension. However, both spatial and spectral stray light coefficients are larger than the simulated value, at 0.05% and 0.09%, respectively. We hypothesize that the main reason is that the diffraction efficiency of the grating's working order (−1st order) is lower than the design, whereas the stray light of the non-working orders is higher than the theory. Another reason is that the surface absorptivity of the machine is not as high as the theory, the measured absorptivity is about 88%; however, this value used for the simulation is 92%.

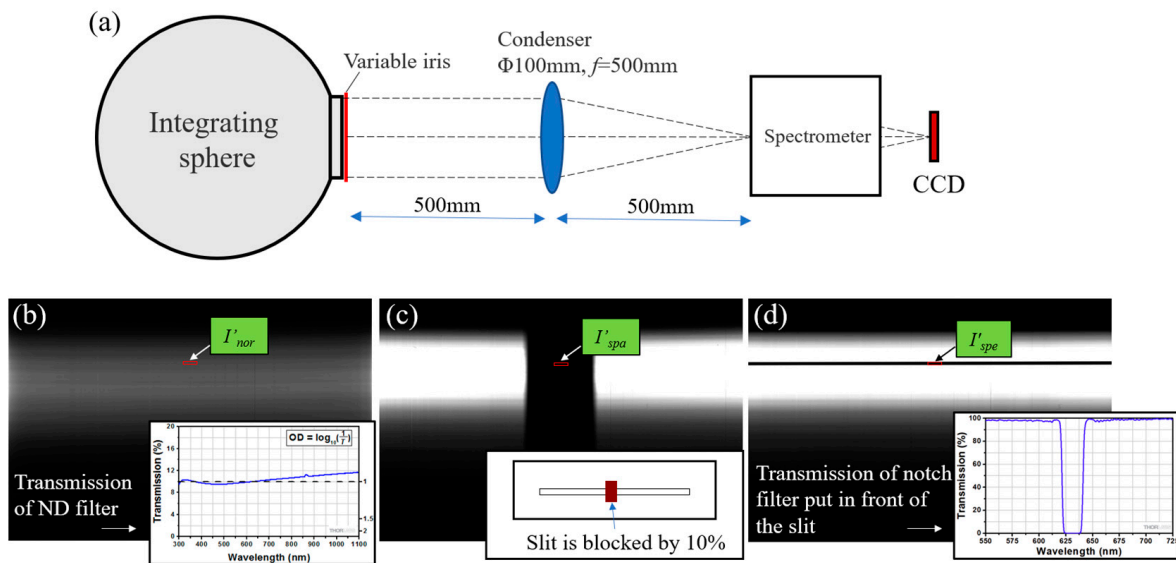


Figure 20. Test of stray light. (a) Schematic diagram of the test device, (b) the image of the spectrometer when a ND filter is put in front of the slit, (c) spatial stray light tested by black spot method, (d) spectral stray light tested using the notch wave method.

The test device for the B3 spectrometer is shown in Figure 21a. A supercontinuum white light laser and an integrating sphere promote uniform illumination at the slit with tunable wavelength. A SWIR T2SL detector is used to acquire spectral lines. Figure 21b shows the spectral lines of 1100 nm, 1700 nm, and 2300 nm. According to the centroid coordinates of spectral lines, the dispersion power of the B3 spectrometer is calculated to be 187.5 nm/mm, and the spectral sampling distance is 12 nm with $2 \times$ pixels binning. Spectral resolutions of two slits show high consistency, as shown in Table 6. The test result of the smile is 1.0% of a pixel, and the keystone is 2.2% of a pixel. The scatter diagram of the 1100 nm spectral line in Figure 21b also shows a slope of about 1.7 pixels, indicating the detector-to-slit rotation during the test process; the slope cannot be directly accounted for as the spectrometer's smile.

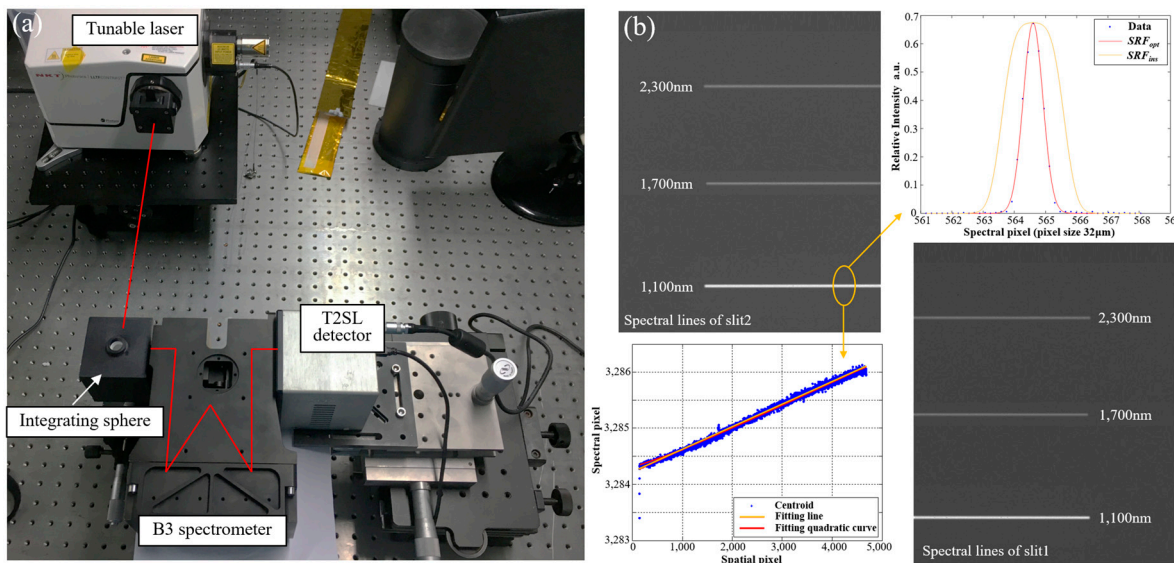


Figure 21. (a) Test device for B3 spectrometer, (b) spectral lines and SRFs of B3 spectrometer.

Table 6. Spectral resolution of B3 spectrometer with 2 × pixels binning.

Wavelength/nm	FWHM of SRF at Different Slits/nm	
	Slit 1	Slit 2
1100	12.1	12.1
1400	12.0	12.0
1700	11.9	11.9
2000	12.0	11.9
2300	12.2	12.1

Test device for the B5 spectrometer is shown in Figure 22a. A high-temperature (800 K) blackbody, three bandpass filters, and a condenser lens are used to illuminate the slit at room temperature, and an uncooled LWIR detector is used. Filters used for testing are 8224 ± 100 nm, 8834 ± 105 nm, and 9350 ± 110 nm, respectively. Figure 22b shows the spectral lines after background rejection. According to the centroid coordinates of spectral lines, the dispersion power of the B5 spectrometer is calculated to be 2052.1 nm/mm, and the spectral sampling distance is 197.0 nm with 3 × pixels binning. The response functions of three spectral lines are shown in Figure 22c, and the raw data contain the filter bandwidth. In order to remove the influence of the filter bandwidth, the transmission function of the filter needs to be deconvoluted. The SRFs after removing the filter bandwidth are shown in Figure 22d, and the spectral resolution of B5 spectrometer is given in Table 7. The spectral resolution is slightly larger than the design. The test results also show that the maximum smile is 2.80% of a pixel, and the keystone is 3.6% of a pixel.

Table 7. Spectral resolution of B5 spectrometer with 3 × pixels binning.

Wavelength/nm	FWHM of SRF at Different Fields/nm			
	−1 Field	0 Field	+1 Field	Average
8224	201.3	201.0	200.9	201.1
8834	202.4	202.1	201.9	202.1
9350	205.9	204.9	204.2	205.0

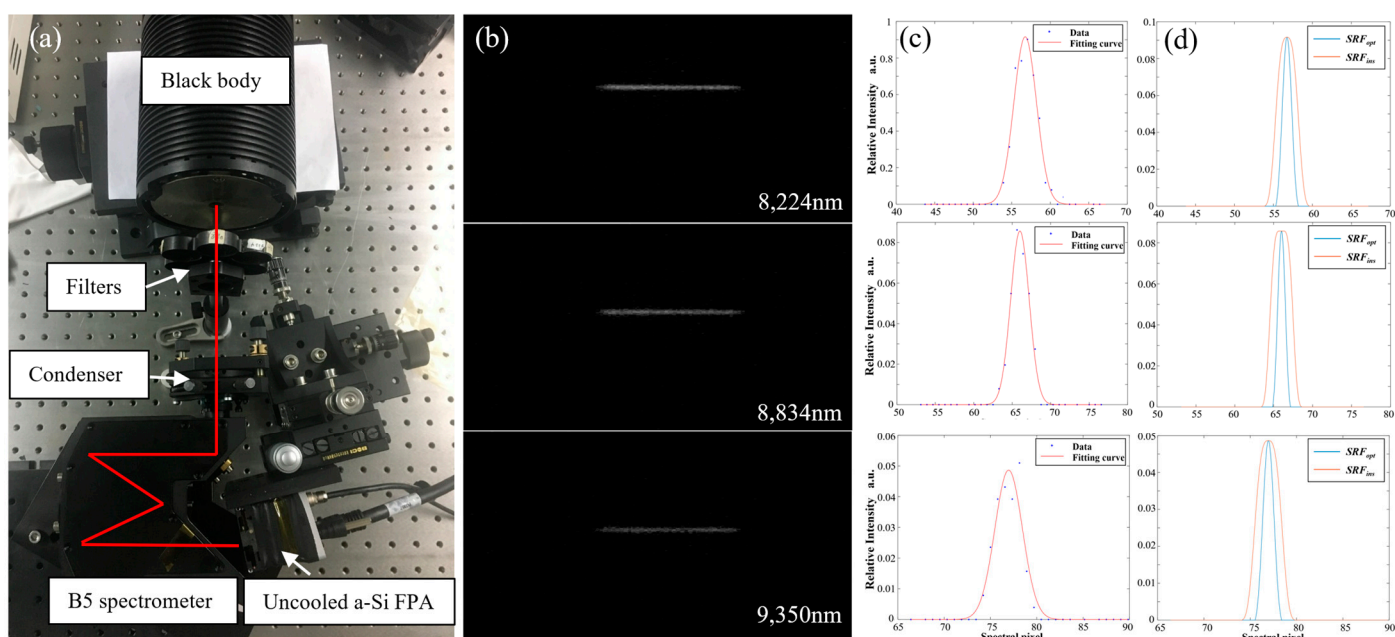


Figure 22. (a) Test device for B5 spectrometer, (b) spectral lines, (c) SRFs containing filter bandwidth, (d) SRF_{opt} and SRF_{ins} of B5 spectrometer.

5. Discussion

At present, there are few reports about full-spectrum hyperspectral remote sensing payloads on geostationary orbit, and we present an optical system, the GeoFWHIS, in this paper. The system comprises an afocal telescope, three imaging objectives, and spectrometers for five bands. The hyperspectral imaging of the ground coverage is completed by internal scanning. The scanning mirror is located in the parallel beam behind the telescope and before the imaging objectives, and this method has the advantage of high stability. Due to the relatively stationary state, the system's need for large relative apertures is not as high as the LEO payloads, which also avoids a larger volume. Design results show that GeoFWHIS has a wide width, high spatial resolution, and excellent spectral imaging performance, which meet the application requirements of continuous monitoring, and fine identification in disaster prevention and mitigation, environment, agriculture, forestry, ocean, meteorology, and resources. We developed prototypes of spectrometers for each sub-band and tested their performance. The results show that the long-slit convex grating spectrometers have high spectral uniformity, minor spectral distortions, high imaging quality, and low stray light. Such high-fidelity performance is also necessary for high-precision quantitative hyperspectral remote sensing.

The GeoFWHIS reported in this paper also has limitations. First, spectrometers are spliced in GeoFWHIS, which greatly reduces the size, difficulty, and cost of spectrometers, but a total of 20 spectrometers will pose other problems. For example, it brings challenges to image stitching and may have the risk of reducing reliability. Secondly, although spectrometers are high-fidelity, it is still not easy to ensure that the performance of different spectrometers in one band is completely consistent. The inconsistencies of slits, gratings, mirrors, and alignment processes all contribute to this difference, leading to the complexity of calibration and the increasing difficulty of image stitching. Therefore, based on the scheme proposed in this paper, reducing the number of spectrometers and adding spectral multiplexing is an optimization direction in the future, which requires the promotion of detector technology simultaneously.

6. Conclusions

In this paper, the optical system of GeoFWHIS is designed and analyzed. The full spectrum of 0.3–12.5 μm is divided into five sub-bands—including UVIS, VNIR, SWIR,

MWIR, and LWIR—which are integrated into the optical system to achieve a 400 km swath, 25–100 m spatial resolution, and 4–200 nm spectral resolution. In each band, four spectrometers are spliced to realize an ultra-long slit, and the total length of the slits is up to 241.3 mm. High-fidelity spectrometers are designed, developed, and tested in this paper. The Offner and Wynne–Offner spectrometers meeting the requirements of long slit and small volume are designed and developed. They have high imaging quality, low spectral distortion, uniform spectral response, and low stray light. The manufactured convex grating has the desired sawtooth groove and high diffraction efficiency; the highest peak efficiency is 86.4%. Test results of the prototypes are consistent with the design and show high fidelity, and all specifications fulfill the requirements. The GeoFWHIS proposed in this paper provides a technical scheme for full-spectrum hyperspectral remote sensing from geostationary orbit. The successful development of full-spectrum high-fidelity spectrometers verifies the feasibility and correctness of the design.

Author Contributions: Writing—original draft: J.Z.; Writing—review and editing, J.Z., Z.Z. and X.C.; Data curation, H.L.; Formal analysis, Z.Z. and H.L.; Investigation, Q.L.; Methodology, Z.Z. and X.C.; Validation, Q.L.; Funding acquisition, J.Z., S.T. and W.S.; Resources, S.T. and W.S.; Project administration, W.S. All authors have read and agreed to the published version of the manuscript.

Funding: This work was supported by the National Natural Science Foundation of China (62105230); National Key Research and Development Program of China (2021YFD2000101, 2016YFB0500501); China Postdoctoral Science Foundation (2020M681700); Priority Academic Program Development of Jiangsu Higher Education Institutions.

Data Availability Statement: No new data were created or analyzed in this study. Data sharing is not applicable to this article.

Acknowledgments: Thanks to Collaborative Innovation Center of Suzhou Nano Science and Technology for its support in the fabrication of the convex gratings.

Conflicts of Interest: The authors declare no conflict of interest.

References

1. Vane, G.; Goetz, A.F.H.; Wellman, J.B. Airborne Imaging Spectrometer: A New Tool for Remote Sensing. *IEEE Trans. Geosci. Remote Sens.* **1984**, *GE-22*, 546–549. [[CrossRef](#)]
2. Green, R.O.; Eastwood, M.L.; Sarture, C.M.; Chrien, T.G.; Aronsson, M.; Chippendale, B.J.; Faust, J.A.; Pavri, B.E.; Chovit, C.J.; Solis, M.; et al. Imaging Spectroscopy and the Airborne Visible/Infrared Imaging Spectrometer (AVIRIS). *Remote Sens. Environ.* **1998**, *65*, 227–248. [[CrossRef](#)]
3. Lucey, P.G.; Horton, K.A.; Williams, T.J.; Hinck, K.; Budney, C.; Rafert, B.; Rusk, T.B. SMIFTS: A cryogenically cooled, spatially modulated imaging infrared interferometer spectrometer. *Proc. SPIE* **1993**, *1937*, 130–141.
4. Hall, J.L.; Boucher, R.H.; Buckland, K.N.; Gutierrez, D.J.; Hackwell, J.A.; Johnson, B.R.; Keim, E.R.; Moreno, N.M.; Ramsey, M.S.; Sivjee, M.G.; et al. MAGI: A New High-Performance Airborne Thermal-Infrared Imaging Spectrometer for Earth Science Applications. *IEEE Trans. Geosci. Remote Sens.* **2015**, *53*, 5447–5457. [[CrossRef](#)]
5. Warren, D.W.; Boucher, R.H.; Gutierrez, D.J.; Keim, E.R.; Sivjee, M.G. MAKO: A high-performance, airborne imaging spectrometer for the long-wave infrared. *Proc. SPIE* **2010**, *7812*, 78120N.
6. Mouroulis, P.; Van Gorp, B.; Green, R.O.; Dierssen, H.; Wilson, D.W.; Eastwood, M.; Boardman, J.; Gao, B.C.; Cohen, D.; Franklin, B.; et al. Portable Remote Imaging Spectrometer Coastal Ocean Sensor: Design, Characteristics, and First Flight Results. *Appl. Opt.* **2014**, *53*, 1363–1380. [[CrossRef](#)]
7. Pearlman, J.S.; Carman, S.L.; Segal, C.C.; Jarecke, P.; Clancy, P.; Browne, W. Overview of the Hyperion Imaging Spectrometer for the NASA EO-1 Mission. In Proceedings of the IGARSS 2001, Scanning the Present and Resolving the Future, IEEE 2001 International Geoscience and Remote Sensing Symposium, Sydney, NSW, Australia, 9–13 July 2001.
8. Pearlman, J.S.; Barry, P.S.; Segal, C.C.; Shepanski, J.; Beiso, D.; Carman, S.L. Hyperion, a Space-Based Imaging Spectrometer. *IEEE Trans. Geosci. Remote Sens.* **2003**, *41*, 1160–1173. [[CrossRef](#)]
9. Rast, M.; Bezy, J.L.; Bruzzi, S. The ESA Medium Resolution Imaging Spectrometer MERIS a Review of the Instrument and Its Mission. *Int. J. Remote Sens.* **1999**, *20*, 1681–1702.
10. Nieke, J.; Borde, F.; Mavrocordatos, C.; Berruti, B.; Delclaud, Y.; Riti, J.B.; Garnier, T. The ocean and land colour imager (OLCI) for the Sentinel 3 GMES mission: Status and first test results. *Proc. SPIE* **2012**, *8528*, 85280C.
11. Lucke, R.L.; Corson, M.; McGlothlin, N.R.; Butcher, S.D.; Wood, D.L.; Korwan, D.R.; Li, R.R.; Snyder, W.A.; Davis, C.O.; Chen, D.T. Hyperspectral Imager for the Coastal Ocean: Instrument Description and First Images. *Appl. Opt.* **2011**, *50*, 1501–1516. [[CrossRef](#)]

12. Pan, Q.; Chen, X.; Zhou, J.; Liu, Q.; Zhao, Z.; Shen, W. Manufacture of the Compact Conical Diffraction Offner Hyperspectral Imaging Spectrometer. *Appl. Opt.* **2019**, *58*, 7298–7304. [[CrossRef](#)] [[PubMed](#)]
13. Guanter, L.; Kaufmann, H.; Segl, K.; Foerster, S.; Rogass, C.; Chabrilat, S.; Kuester, T.; Hollstein, A.; Rossner, G.; Chlebek, C.; et al. The EnMAP Spaceborne Imaging Spectroscopy Mission for Earth Observation. *Remote Sens.* **2015**, *7*, 8830–8857. [[CrossRef](#)]
14. Peschel, T.; Beier, M.; Damm, C.; Hartung, J.; Jende, R.; Müller, S.; Rohde, M.; Gebhardt, A.; Risse, S.; Walter, I.; et al. Integration and testing of an imaging spectrometer for earth observation. *Proc. SPIE* **2018**, *11180*, 111800O-2.
15. Mouroulis, P.; Green, R.O.; Van, G.B.; Moore, L.B.; Wilson, D.W.; Bender, H.A. Landsat Swath Imaging Spectrometer Design. *Opt. Eng.* **2016**, *55*, 015104. [[CrossRef](#)]
16. Cogliati, S.; Sarti, F.; Chiarantini, L.; Cosi, M.; Lorusso, R.; Lopinto, E.; Miglietta, F.; Genesio, L.; Guanter, L.; Damm, A.; et al. The PRISMA Imaging Spectroscopy Mission: Overview and First Performance Analysis. *Remote Sens. Environ.* **2021**, *262*, 112499. [[CrossRef](#)]
17. Lockwood, R.B.; Cooley, T.W.; Nadile, R.M.; Gardner, J.A.; Armstrong, P.S.; Payton, A.M.; Davis, T.M.; Straight, S.D. Advanced responsive tactically effective military imaging spectrometer (ARTEMIS): System overview and objectives. *Proc. SPIE* **2007**, *6661*, 666102.
18. Zeng, C.; Han, Y.; Liu, B.; Sun, P.; Li, X.; Chen, P. Optical Design of a High-Resolution Spectrometer with a Wide Field of View. *Opt. Lasers Eng.* **2021**, *140*, 106547. [[CrossRef](#)]
19. Dwight, J.G.; Tkaczyk, T.S.; Alexander, D.; Pawlowski, M.E.; Stoian, R.-I.; Luvall, J.C.; Tatum, P.F.; Jedlovec, G.J. Compact Snapshot Image Mapping Spectrometer for Unmanned Aerial Vehicle Hyperspectral Imaging. *J. Appl. Rem. Sens.* **2018**, *12*, 044004. [[CrossRef](#)]
20. Mu, T.; Han, F.; Li, H.; Tuniyazi, A.; Li, Q.; Gong, H.; Wang, W.; Liang, R. Snapshot Hyperspectral Imaging Polarimetry with Full Spectropolarimetric Resolution. *Opt. Lasers Eng.* **2022**, *148*, 106767. [[CrossRef](#)]
21. Bourdarot, G.; Le Coarer, E.; Bonfils, X.; Alecian, E.; Rabou, P.; Magnard, Y. NanoVipa: A Miniaturized High-Resolution Echelle Spectrometer, for the Monitoring of Young Stars from a 6U Cubesat. *CEAS Space J.* **2017**, *9*, 411–419. [[CrossRef](#)]
22. Zhu, J.; Shen, W. Analytical Design of Athermal Ultra-Compact Concentric Catadioptric Imaging Spectrometer. *Opt. Express* **2019**, *27*, 31094–31109. [[CrossRef](#)] [[PubMed](#)]
23. Chrisp, M.P.; Lockwood, R.B.; Smith, M.A.; Balonek, G.; Holtsberg, C.; Thome, K.J.; Murray, K.E.; Ghuman, P. Development of a Compact Imaging Spectrometer Form for the Solar Reflective Spectral Region. *Appl. Opt.* **2020**, *59*, 10007. [[CrossRef](#)] [[PubMed](#)]
24. Cook, L.G.; Silny, J.F. Imaging spectrometer trade studies: A detailed comparison of the Offner-Chrisp and reflective triplet optical design forms. *Proc. SPIE* **2010**, *7813*, 78130F.
25. Yuan, L.; He, Z.; Lv, G.; Wang, Y.; Li, C.; Xie, J.; Wang, J. Optical design, laboratory test, and calibration of airborne long wave infrared imaging spectrometer. *Opt. Express* **2017**, *25*, 22440–22454. [[CrossRef](#)] [[PubMed](#)]
26. Krimchansky, A.; Machi, D.; Cauffman, S.A.; Davis, M.A. Next-generation geostationary operational environmental satellite (GOES-R series): A space segment overview. *Proc. SPIE* **2004**, *5570*, 155–164.
27. Aminou, D.M.A.; Jacquet, B.; Pasternak, F. Characteristics of the meteosat second generation (MSG) radiometer/imager: SEVIRI. *Proc. SPIE* **1997**, *3221*, 19–31.
28. Vaillon, L.; Schull, U.; Knigge, T.; Bevilion, C. Geo-Oculus: High resolution multi-spectral Earth imaging mission from geostationary orbit. *Proc. SPIE* **2010**, *10565*, 105651V-2.
29. Elwell, J.D.; Cantwell, G.W.; Scott, D.K.; Esplin, R.W.; Hansen, G.B.; Jensen, S.M.; Jensen, M.D.; Brown, S.B.; Zollinger, L.J.; Thurgood, V.A.; et al. A Geosynchronous Imaging Fourier Transform Spectrometer (GIFTS) for Hyperspectral Atmospheric Remote Sensing: Instrument Overview and Preliminary Performance Results. *Proc. SPIE* **2006**, *6297*, 62970S.
30. Tuffiaro, N.; Davis, C.O.; Valle, T.; Good, W.; Stephens, M.; Spuhle, R.P. Behavioral Model and Simulator for the Multi-Slit Optimized Spectrometer (MOS). *Proc. SPIE* **2013**, *8870*, 88700E-1.
31. Butz, A.; Orphal, J.; Checa-Garcia, R.; Friedl-Vallon, F.; von Clarmann, T.; Bovensmann, H.; Hasekamp, O.; Landgraf, J.; Knigge, T.; Weise, D.; et al. Geostationary Emission Explorer for Europe (G3E): Mission Concept and Initial Performance Assessment. *Atmos. Meas. Technol.* **2015**, *8*, 4719–4734. [[CrossRef](#)]
32. Choi, W.J.; Moon, K.J.; Yoon, J.; Cho, A.; Kim, S.; Lee, S.; Ko, D.H.; Kim, J.; Ahn, M.H.; Kim, D.R.; et al. Introducing the Geostationary Environment Monitoring Spectrometer. *J. Appl. Rem. Sens.* **2018**, *12*, 0044005. [[CrossRef](#)]
33. Polonsky, I.N.; O'Brien, D.M.; Kumer, J.B.; O'Dell, C.W.; the geoCARB Team. Performance of a geostationary mission, geoCARB, to measure CO₂, CH₄ and CO column-averaged concentrations. *Atmos. Meas. Technol.* **2014**, *7*, 959–981. [[CrossRef](#)]
34. Kolm, M.G.; Maurer, R.; Sallusti, M.; Bagnasco, G.; Gulde, S.T.; Smith, D.J.; Bazalgette, C.G. Sentinel 4: A geostationary imaging UVN spectrometer for air quality monitoring: Status of design, performance and development. *Proc. SPIE* **2014**, *10563*, 1056341.
35. Zoogman, P.; Liu, X.; Suleiman, R.M.; Pennington, W.F.; Flittner, D.E.; Al-Saadi, J.A.; Hilton, B.B.; Nicks, D.K.; Newchurch, M.J.; Carr, J.L.; et al. Tropospheric Emissions: Monitoring of Pollution (TEMPO). *J. Quant. Spectrosc. Radiat. Transf.* **2017**, *186*, 17–39. [[CrossRef](#)]
36. Lu, F.; Shou, Y. Channel Simulation for FY-4 AGRI. In Proceedings of the 2011 IEEE International Geoscience and Remote Sensing Symposium, Vancouver, BC, Canada, 24–29 July 2011; pp. 3265–3268.
37. Liu, Y.N.; Sun, D.X.; Hu, X.N.; Ye, X.; Li, Y.D.; Liu, S.F.; Cao, K.Q.; Chai, M.Y.; Zhou, W.Y.N.; Zhang, J.; et al. The Advanced Hyperspectral Imager: Aboard China's GaoFen-5 Satellite. *IEEE Geosci. Remote Sens. Mag.* **2019**, *7*, 23–32. [[CrossRef](#)]

38. Li, Q.; Han, L.; Jin, Y.M.; Shen, W.M. Afocal three-mirror anastigmat with zigzag optical axis for widened field of view and enlarged aperture. *Proc. SPIE* **2016**, *9618*, 96180D.
39. Mouroulis, P.; McKerns, M.M. Pushbroom Imaging Spectrometer with High Spectroscopic Data Fidelity: Experimental Demonstration. *Opt. Eng.* **2000**, *39*, 808–816. [[CrossRef](#)]
40. Mouroulis, P.; Green, R.O. Review of High Fidelity Imaging Spectrometer Design for Remote Sensing. *Opt. Eng.* **2018**, *57*, 040901. [[CrossRef](#)]
41. Kwo, D.; Lawrence, G.; Chrisp, M. Design of a grating spectrometer from a 1:1 Offner mirror system. *Proc. SPIE* **1987**, *818*, 275–279.
42. Prieto-Blanco, X.; de la Fuente, R. Compact Offner–Wynne Imaging Spectrometers. *Opt. Commun.* **2014**, *328*, 143–150. [[CrossRef](#)]
43. Zhu, J.; Shen, W. Design and Manufacture of Compact Long-Slit Spectrometer for Hyperspectral Remote Sensing. *Optik* **2021**, *247*, 167896. [[CrossRef](#)]
44. Reimers, J.; Bauer, A.; Thompson, K.P.; Rolland, J.P. Freeform Spectrometer Enabling Increased Compactness. *Light Sci. Appl.* **2017**, *6*, e17026. [[CrossRef](#)]
45. Zhu, J.; Chen, X.; Zhao, Z.; Shen, W. Design and Manufacture of Miniaturized Immersed Imaging Spectrometer for Remote Sensing. *Opt. Express* **2021**, *29*, 22603–22613. [[CrossRef](#)] [[PubMed](#)]
46. Montero-Orille, C.; Prieto-Blanco, X.; González-Núñez, H.; de la Fuente, R. Design of Dyson Imaging Spectrometers Based on the Rowland Circle Concept. *Appl. Opt.* **2011**, *50*, 6487–6494. [[CrossRef](#)] [[PubMed](#)]
47. Van, G.B.; Mouroulis, P.; Wilson, D.W.; Green, R.O. Design of the compact wide swath imaging spectrometer (CWIS). *Proc. SPIE* **2014**, *9222*, 92220C.
48. Chrisp, M.P. Imaging Spectrometer Wide Field Catadioptric Design. US Patent 7414719B, 19 August 2008.
49. Prieto-Blanco, X.; Montero-Orille, C.; Couce, B.; de la Fuente, R. Analytical Design of an Offner Imaging Spectrometer. *Opt. Express* **2006**, *14*, 9156–9168. [[CrossRef](#)]
50. Zhu, J.; Chen, X.; Zhao, Z.; Shen, W. Long-Slit Polarization-Insensitive Imaging Spectrometer for Wide-Swath Hyperspectral Remote Sensing from a Geostationary Orbit. *Opt. Express* **2021**, *29*, 26851–26864. [[CrossRef](#)]
51. Reimers, J.; Thompson, K.; Whiteaker, K.L.; Rolland, J.P. Spectral full-field displays for spectrometers. *Proc. SPIE* **2014**, *9293*, 92930O.
52. Cobb, J.M.; Comstock, L.E.; Dewa, P.G.; Dunn, M.M.; Flint, S.D. Innovative manufacturing and test technologies for imaging hyperspectral spectrometers. *Proc. SPIE* **2006**, *6233*, 62330R.
53. Beier, M.; Hartung, J.; Peschel, T.; Damm, C.; Gebhardt, A.; Scheiding, S.; Stumpf, D.; Zeitner, U.D.; Risse, S.; Eberhardt, R.; et al. Development, Fabrication, and Testing of an Anamorphic Imaging Snap-Together Freeform Telescope. *Appl. Opt.* **2015**, *54*, 3530–3542. [[CrossRef](#)]

Disclaimer/Publisher’s Note: The statements, opinions and data contained in all publications are solely those of the individual author(s) and contributor(s) and not of MDPI and/or the editor(s). MDPI and/or the editor(s) disclaim responsibility for any injury to people or property resulting from any ideas, methods, instructions or products referred to in the content.